Journal of Computational Physics 230 (2011) 1865–1875

Contents lists available at ScienceDirect

Journal of Computational Physics

journal homepage: www.elsevier.com/locate/jcp

Method for efficient prevention of gravity wave decoupling on rectangular semi-staggered grids

Slobodan Nickovic [a], Vladimir Djurdjevic [b,c,*], Mirjam Vujadinovic [b,c,d], Zavisa I. Janjic [e], Milan Curcic [f], Borivoj Rajkovic [b]

[a] World Meteorological Organization, 7bis, Avenue de la Paix, 2000 Geneva, Switzerland
[b] Institute of Meteorology, Faculty of Physics, University of Belgrade, Dobracina 16, 11000 Belgrade, Serbia
[c] South East European Virtual Climate Change Center, Bulevar Oslobodjenja 8, 11000 Belgrade, Serbia
[d] Faculty of Agriculture, University of Belgrade, Nemanjina 6, 11080 Belgrade, Serbia
[e] National Centers for Environmental Prediction, 5200 Auth Road Camp Springs, Maryland 20746, USA
[f] Rosenstiel School of Marine and Atmospheric Science, University of Miami, 4600 Rickenbacker Causeway, Miami, USA

ARTICLE INFO

Article history:
Received 3 June 2010
Received in revised form 22 November 2010
Accepted 24 November 2010
Available online 1 December 2010

Keywords:
Gravity wave
Rectangular grid
Divergence correction

ABSTRACT

Generation of short gravity wave noise often occurs on semi-staggered rectangular grids as a result of sub-grid decoupling when there is a strong forcing in the mass field. In this study a numerical scheme has been proposed to prevent the generation of the gravity wave decoupling. The proposed numerical method provides efficient communication between decoupled gravity wave finite-difference solutions by a simple averaging of a term in the height tendency in the continuity equation. The proposed method is tested using a shallow water sink model developed for the purpose of this study. It has been demonstrated that this method outperforms other existing approaches. The new scheme is time efficient, based on explicit time integration and can be easily implemented. The proposed method is applicable in hydrodynamic models specified on semi-staggered B or E grids.

1. Introduction

The choice of horizontal computational grids is an important issue in modeling the geophysical fluid dynamics, especially for simulation of processes where horizontal scales dominate over the vertical. A typical example of such dynamics is a quasi-horizontal process of geostrophic adjustment in atmospheric and oceanic flows.

Rectangular horizontal grids are most frequently used in hydrodynamic modelling applications (these are grids in which model variables are located in grid rectangles). Winninghoff [17] and Arakawa [2] suggested five rectangular distributions of model variables, i.e. the A, B, C, D and E grid. These grids are drawn in Fig. 1 with a common shortest distance ***d*** between grid points carrying the same variable. Although these distributions were proposed for atmospheric modeling, they can be used in other dynamic modeling applications, e.g. in oceanography, hydrology, electromagnetic dynamics, and others. Alternatively, grid structures for horizontal variable distribution other than rectangular, such as hexagonal grids [13,16] could also be used.

Accumulated scientific evidence, primarily in atmospheric and oceanic modelling, indicates that different rectangular horizontal grids do not have same properties for simulation of various components of the atmospheric motions. Studies

* Corresponding author at: Institute of Meteorology, Faculty of Physics, University of Belgrade, Dobracina 16, 11000 Belgrade, Serbia.
E-mail address: vdj@ff.bg.ac.rs (V. Djurdjevic).

0021-9991/$ - see front matter © 2010 Elsevier Inc. All rights reserved.
doi:10.1016/j.jcp.2010.11.037

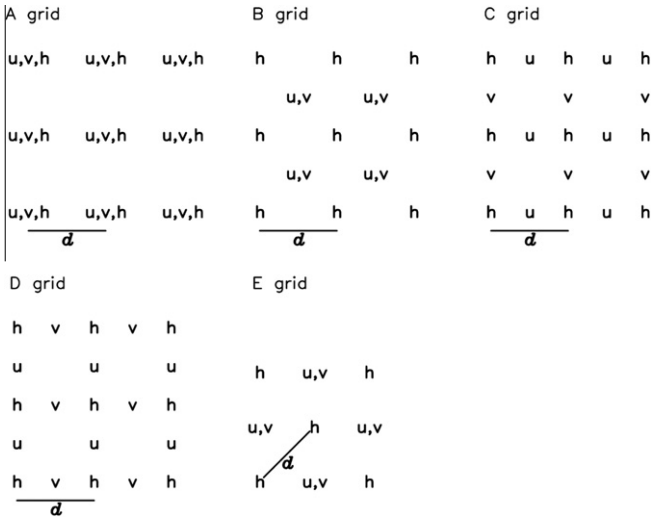

Fig. 1. Distribution of variables on the A, B, C, D and E grids, with equal grid distance d for all grids.

show that the C, B and E grids are more appropriate than others, although each of them is still experiencing some numerical difficulties [9]. It has been demonstrated that the B and E grids are geometrically and dynamically equivalent [10]. Therefore, all conclusions for the B grid that are presented in this paper can be applied for the E grid as well.

The problem on the C grid is a consequence of the velocity spatial averaging when calculating the Coriolis force term in the discretized shallow water equations system. The problem appears for all wavelengths of small Rossby radius of deformation [2]. Also, in case of a stratified fluid, C grid can have numerical problems if there is a weak stability and when the horizontal grid resolution is two orders of magnitude higher than the vertical grid one [9].

On the other hand, the B grid has difficulties with simulation of the shortest gravity and gravity-inertia waves, in particular the external and fast internal gravity modes. However, unlike on the C grid, on the B grid the problem is restricted to the shortest waves. The cause of the problem is the use of the B grid finite-difference averaging operators in the continuity equation [9]. As a consequence, a height disturbances generated, e.g. in a computational height point cannot propagate to the nearest neighboring height points. This leads to the decoupling of the gravity wave solution and generation of numerical, low-frequency, short-wave noise. In response to this problem, one sided TASU differencing scheme [2], and techniques that modify the acceleration [12] or correct the calculation of the finite-difference divergence [7,8,10] have been developed which to a large extent overcome this numerical problem. A new technique that is proposed in this study is compared with previous ones, and it is shown that the short wave noise generation by the propagation of the gravity waves is more effectively controlled.

2. Gravity and inertia wave dispersion and related numerical problems

The shallow water equations are often used to investigate basic motion features of geophysical fluids. The linearized shallow water equation system which contains only gravity and inertia wave motions has the form:

$$\begin{aligned}\frac{\partial u}{\partial t} &= -g\frac{\partial h}{\partial x} + f v,\\ \frac{\partial v}{\partial t} &= -g\frac{\partial h}{\partial y} - f u,\\ \frac{\partial h}{\partial t} &= -H\left(\frac{\partial u}{\partial x} + \frac{\partial v}{\partial y}\right),\end{aligned} \tag{1}$$

where u and v are horizontal velocity components, g is the gravity, h is the height perturbation and H is the height of the basic state.

The non-staggered A grid and the staggered D grid in the Arakawa notation [2] appear to be inferior compared to the remaining possibilities considered – the staggered C grid and the semi-staggered B and E grids.

As can be inferred from Fig. 2, the E grid can be considered as a combination of two C grids shifted relative to each other by an E grid distance. Namely, the two C grids (playing a role of subgrids of the E grid) are denoted in the figure with black- and red-colored model variables. Also, semi-staggered E grid, can be obtained by rotating the B grid by $\pi/4$, and vice versa. Therefore, B grid can be considered as a combination of a two C subgrids rotated by $\pi/4$.

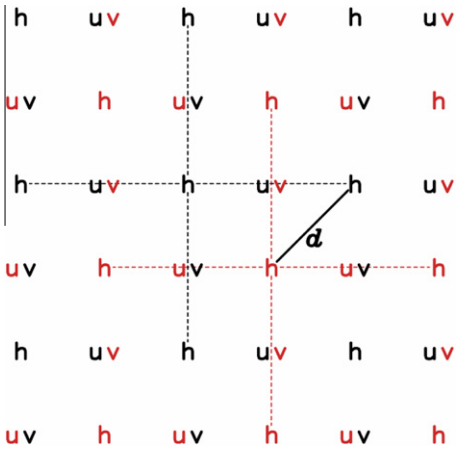

Fig. 2. Two C grids, playing a role of subgrids of the E grid, denoted with black- and red-colored variables. Dashed lines connect neighboring points from the same C grid. E grid horizontal step is represented by solid line marked with *d*. (For interpretation of the references to color in this figure legend, the reader is referred to the web version of this article.)

The finite difference forms of the Eq. (1) for the grids B and C are respectively,

$$\begin{aligned}\frac{\partial u}{\partial t} &= -g\overline{\delta_x h}^{y} + f v,\\ \frac{\partial v}{\partial t} &= -g\overline{\delta_y h}^{x} - f u,\\ \frac{\partial h}{\partial t} &= -H(\overline{\delta_x u}^{y} + \overline{\delta_y v}^{x})\end{aligned} \tag{2$_B$}$$

and

$$\begin{aligned}\frac{\partial u}{\partial t} &= -g\delta_x h + f\bar{v}^{xy},\\ \frac{\partial v}{\partial t} &= -g\delta_y h - f\bar{u}^{xy},\\ \frac{\partial h}{\partial t} &= -H(\delta_x u + \delta_y v).\end{aligned} \tag{2$_C$}$$

The central finite-differences operators are defined as:

$$\begin{aligned}\delta_s\alpha &= \frac{\alpha\left(s+\frac{\Delta s}{2}\right) - \alpha\left(s-\frac{\Delta s}{2}\right)}{\Delta s}\\ \bar{\alpha}^{s} &= \frac{\alpha\left(s+\frac{\Delta s}{2}\right) + \alpha\left(s-\frac{\Delta s}{2}\right)}{2},\end{aligned} \tag{3}$$

where Δs is the distance between two neighboring grid points carrying the same variable in the direction of the coordinate axis s.

Following [3], in order to investigate the behavior of the (1), (2)$_B$ and (2)$_C$, we introduce a wave-like solution

$$\alpha = \hat{\alpha}e^{i(kx+ly-\nu t)}, \tag{4}$$

where $\hat{\alpha}$ is the amplitude of the variable α, $k = 2\pi/L_x$ and $l = 2\pi/L_y$ are wave numbers in the x and y directions, respectively, and $\nu = 2\pi/T$ is the frequency. The notation $X = k\mathrm{d}$ and $Y = ld$ is used for simplicity. Substitution of (4) into (1), (2)$_B$ and (2)$_C$ leads to the expressions for continuous and discrete gravity-inertia relative frequencies:

$$\left(\frac{\nu}{f}\right)^2 = 1 + \kappa^2(X^2 + Y^2), \tag{5$_{Cont}$}$$

$$\left(\frac{\nu}{f}\right)^2 = \cos^2\left(\frac{X}{2}\right)\cos^2\left(\frac{Y}{2}\right) + 4\kappa^2\left[\sin^2\left(\frac{X}{2}\right) + \sin^2\left(\frac{Y}{2}\right)\right], \tag{5$_C$}$$

$$\left(\frac{\nu}{f}\right)^2 = 1 + 4\kappa^2\left[\sin^2\left(\frac{X}{2}\right)\cos^2\left(\frac{Y}{2}\right) + \cos^2\left(\frac{X}{2}\right)\sin^2\left(\frac{Y}{2}\right)\right], \tag{5$_B$}$$

where $\kappa \equiv \frac{\sqrt{gH}/f}{d}$ is the non-dimensional Rossby radius of deformation.

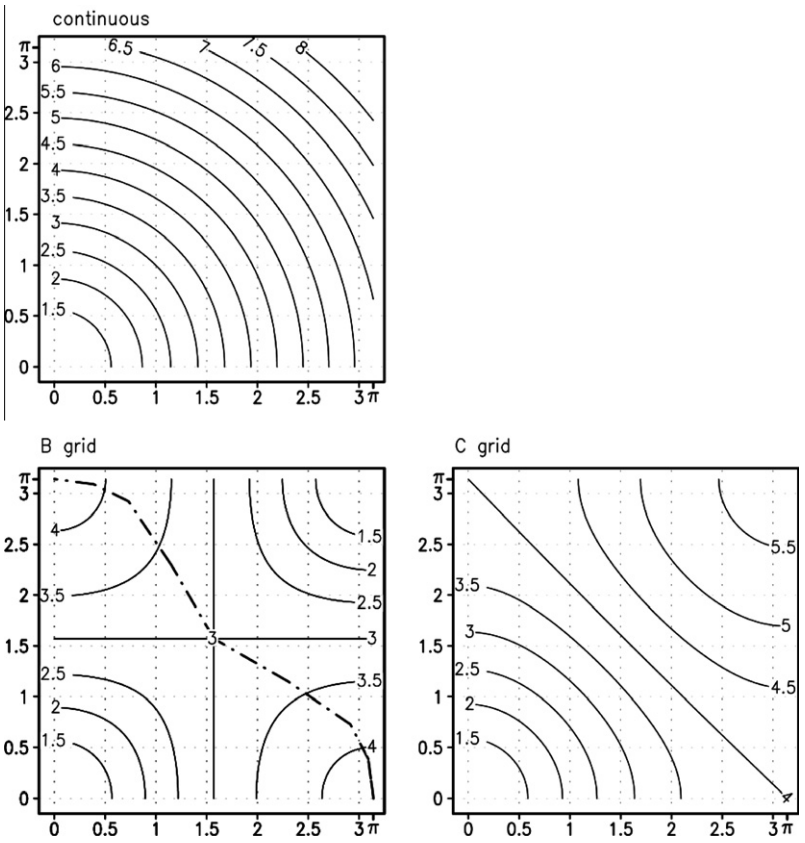

Fig. 3. Normalized frequencies in the first quadrant of the admissible wave numbers domain in continues case, B and C grid.

The normalized frequencies $|v|/f$, calculated from relations (5) for $\kappa = 2$, are plotted in Fig. 3 [3]. Since the frequencies are symmetric, they are presented only for the first quadrant of the *XY* coordinate system in the continuous case, and for the first quadrant of the admissible wave number range for the discrete cases.

Fig. 3 shows that the continuous gravity-inertia frequency is an isotropic and monotonic function increasing with the increase of the intensity of the wave number vector. Therefore, the first derivative of frequency, i.e. the group velocity of waves, is always positive. In the finite difference form, C grid generally correctly reproduces monotonic character of the frequency and thus successfully simulates the sign of the group velocity [3]. However, there is a potential numerical problem that may occur if κ approaches 1. In that case we obtain

$$\left(\frac{v}{f}\right)^2 = \cos^2\left(\frac{X}{2}\right) + \sin^2\left(\frac{X}{2}\right) = 1. \tag{6}$$

The gravity-inertia frequency in this case is falsely represented as the inertial frequency in the whole wave domain and for all wave components. The case $\kappa \approx 1$ corresponds to the low Rossby radius of deformation. Extended inspection of the equation system for stratified fluids [9], shows that C grid might experience difficulties in the two cases: when there is a weak stability or when the ratio between horizontal and vertical grid intervals is on the order of 100. Of course, the problem also may occur in case of slow higher internal modes with their corresponding small equivalent mean heights.

Opposite to the C grid and the continuous case, there is an area on the diagram for the B grid where frequency is decreasing with increasing wave number (Fig. 3) [3]. The dot-dashed line connects points in which frequency starts to decrease with increasing wave numbers, for a constant *X*/*Y*. In the (π, π) corner point of the permissible wave domain which corresponds to the shortest two-grid interval wave, gravity-inertia frequency for the B grid drops to 1. In case of pure gravity waves this means that the two-grid-interval gravity wave becomes stationary. To inspect the origin of the stationary character of the two-grid-interval gravity wave, we simplify the system by dropping the Coriolis terms in $(2)_B$. Then, the resulting wave equation for h is:

$$\frac{\partial^2 h}{\partial t^2} = -gH\left(\overline{\delta_{xx}h}^{yy} + \overline{\delta_{yy}h}^{xx}\right).$$

The form of this equation indicates that a gravity wave generated in one computational height point can propagate only within one C subgrid in which the point of the disturbance belongs. In the wave spectrum generated in this way, the shortest

resolvable wave is stationary, as concluded above. In the case of a disturbance distributed over multiple points belonging to both subgrids, the existence of stationary solutions with different height amplitudes will result to a standing two-grid-interval-wave noise. Formation of such noise during numerical integration will be demonstrated in the next section.

3. Numerical techniques for preventing the short-wave noise

The grid decoupling problem has been traditionally dealt with using smoothing and/or filtering which have been effective in removing the small scale noise. Thus, the grid decoupling have not received much visibility. We want to attack the problem at its root, without affecting other equation terms/processes, and therefore, here we will consider only the techniques following the same approach.

3.1. Shallow-water equation model

A small scale, including single-point forcing is the most explicit cause of wave decoupling in numerical hydrodynamic models. In numerical weather prediction models, such forcing may be induced by topography or by convective and grid scale cloud process, while in hydrologic models, small-scale forcing is typically generated by localized precipitation input. In order to test the performance of some techniques for suppression of gravity wave decoupling on the B grid, a barotropic, linearized, shallow water equation model with a single point source forcing is designed. We focus on the single point forcing because it illustrates the problem in a simple and clear way, and because this is the most difficult problem that can be (and is) encountered in practice.

Pure gravity and gravity-inertia waves are integrated in a square domain of 1010 km $\times$ 1010 km size, with grid spacing of $d =$ 10 km and a flat bottom. The initial state of the fluid is steady with the mean free surface height of $H = 10$ m. The constant source forcing is introduced in the central computational height point with the intensity of 1.5 mm min^{-1}.

The time step in all experiments is 90% of the longest time step allowed by the linear numerical stability criterion. The integration time for all experiments is 24 h. Within the period of the simulation, the wave front does not reach lateral model boundaries. Therefore constant boundary conditions are applied.

The forward–backward time-integration scheme [1,5,8] is used for gravity wave terms, and a trapezoidal time scheme is applied for the Coriolis terms [6]. The finite difference Eq. $(2)_B$ then become:

$$\begin{aligned} u^{n+1} &= u^n + \Delta t g(\overline{\delta_x h}^y)^{n+1} + \frac{\Delta t f}{2}(v^n + v^{n+1}),\\ v^{n+1} &= v^n + \Delta t g(\overline{\delta_y h}^x)^{n+1} - \frac{\Delta t f}{2}(u^n + u^{n+1}),\\ h^{n+1} &= h^n - \Delta t H(\overline{\delta_x u}^y - \overline{\delta_y v}^x)^n + G + C, \end{aligned} \tag{7}$$

where G denotes the source term and C is the term representing one of techniques for controlling the separation of gravity waves on the B grid mentioned above. Note that Randal [15] proposed that modified B grid and shallow water equations be used in order to avoid the grid separation, while Kar [11] addressed an analogous problem on the A grid.

3.2. Experiments with no short-wave suppression

In the absence of any action to suppress the wave decoupling, a short wave noise is generated in a variety of forms, as our shallow water experiments show (Fig. 4). The existence of the short-wave noise is evident in the height field in both, gravity and gravity-inertia case experiments. Small-scale curly structures on stream lines, clearly visible in the figure, represent noise in the velocity field.

3.3. Experiments with divergence correction

Different methods have been developed to overcome the short-wave noise problem on semi-staggered grids. Mesinger [12] proposed an acceleration modification technique based on linear equations, as a way to control the grid separation problem for the B/E grid. In a more general approach that included nonlinear dynamics, Janjic [7,8] introduced a technique based on the divergence correction in the continuity equation that suppresses generation of short waves. The two techniques are equivalent for the governing linear gravity wave equations without advection. A similar technique for the A grid was proposed by Kar [11].

Following [8], we describe the divergence correction approach on the B grid starting from the equations set in which the Coriolis terms are neglected:

$$\begin{aligned} u^{n+1} &= u^n - \Delta t g(\overline{\delta_x h}^y)^{n+1},\\ v^{n+1} &= v^n - \Delta t g(\overline{\delta_y h}^x)^{n+1},\\ h^{n+1} &= h^n - \Delta t H(\nabla_* \cdot \mathbf{v})^n_x. \end{aligned} \tag{8}$$

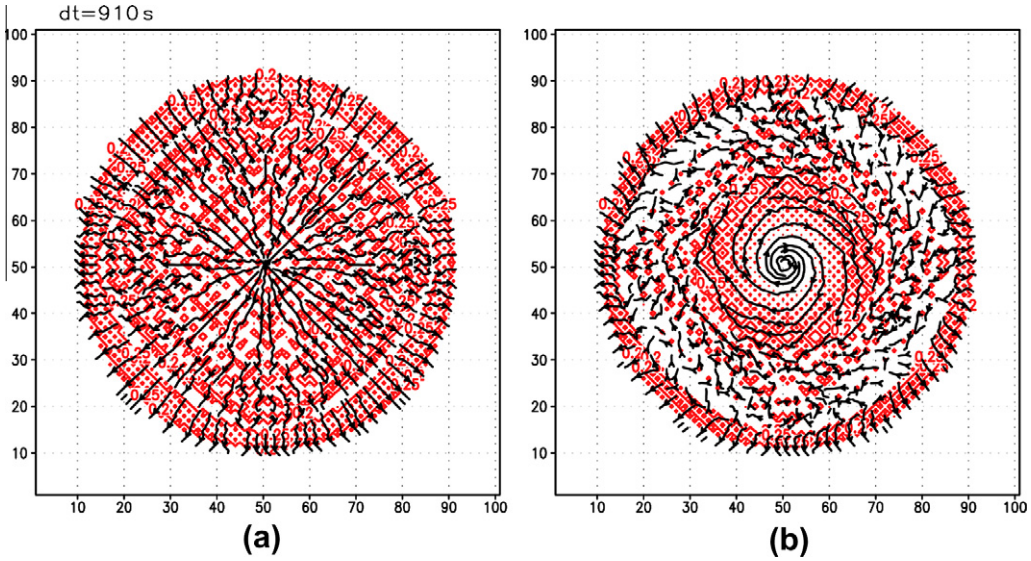

Fig. 4. Source experiments with no intervention in the continuity equation for preventing wave decoupling, in case of pure gravity waves (panel a) and gravity-inertia waves (panel b). Black lines denote streamlines, while red contours represent fluid height. (For interpretation of the references to color in this figure legend, the reader is referred to the web version of this article.)

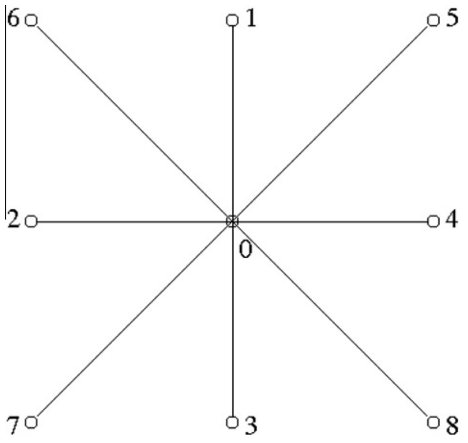

Fig. 5. Grid point notation used for defining $\nabla^2_\times$ and ∇^2_+ Laplacians.

The divergence in $(8)_3$ is defined using the following approximation

$$(\nabla_* \cdot \mathbf{v})^n_x \equiv (\nabla_* \cdot \mathbf{v})^{n-1} - \Delta t g \left[(1-w)\nabla^2_\times + w\nabla^2_+ \right] h^n. \tag{9}$$

Using the grid point notation in Fig. 5, two finite-difference Laplacian operators are defined as:

$$\begin{aligned} \nabla^2_\times h &= \frac{h_5 + h_6 + h_7 + h_8 - 4h_0}{d^2}, \\ \nabla^2_+ h &= \frac{h_1 + h_2 + h_3 + h_4 - 4h_0}{2d^2}. \end{aligned} \tag{10}$$

Applying the operator ∇_* to $(8)_1$ and $(8)_2$, one obtains

$$(\nabla_* \cdot \mathbf{v})^n = (\nabla_* \cdot \mathbf{v})^{n-1} - \Delta t g \nabla^2_\times h^n. \tag{11}$$

Substitution of (11) into (9) leads to:

$$(\nabla_* \cdot \mathbf{v})^n_x = (\nabla_* \cdot \mathbf{v})^{n-1} - \Delta t g \nabla^2_\times h^n - \Delta t w g \left(\nabla^2_+ - \nabla^2_\times \right) h^n \tag{12}$$

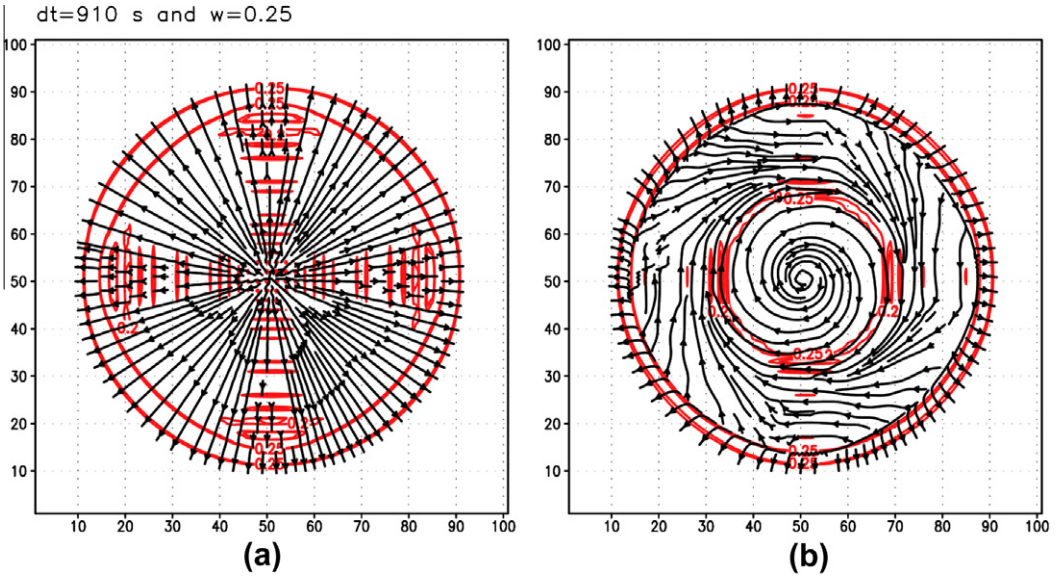

Fig. 6. The same as Fig. 4 but with the generalized divergence correction applied.

and

$$(\nabla_* \cdot \mathbf{v})_x^n = (\nabla_* \cdot \mathbf{v})^n - \Delta t w g \left(\nabla_+^2 - \nabla_\times^2\right) h^n. \tag{13}$$

Finally, the continuity equation takes the form:

$$h^{n+1} = h^n - \Delta t H (\overline{\delta_x u}^y + \overline{\delta_y v}^x)^n + (\Delta t)^2 w g H \left(\nabla_+^2 - \nabla_\times^2\right) h^n. \tag{14}$$

The only difference between $(8)_3$ and (14) is the appearance of the Laplacian term on the right-hand side in the latter equation. This term does not affect the mass conservation. The Courant–Friedrichs–Levy (CFL) stability criterion of the original forward–backward scheme is not affected by the divergence correction if w does not exceed 0.25 [8]. Since the correction term has a higher order of Δt than the mass divergence term, the divergence correction technique is dependent on the time step. To avoid this problem, a generalized divergence correction has been developed [10]. In this method, a grid point height h_*^n is defined as a linear combination of the height at the grid point considered, and the value h'^n obtained by a fourth order interpolation from the surrounding points:

$$h^{n^*} = \alpha h^n + (1-\alpha) h'^n. \tag{15}$$

Using the notation of grid points in Fig. 5, and after some algebraic evaluation one obtains

$$h_0^{n^*} = h_0^n + \frac{1-\alpha}{2}\left[(h_5 + h_6 + h_7 + h_8 - 4h_0) - \frac{1}{2}(h_1 + h_2 + h_3 + h_4 - 4h_0)\right]^n. \tag{16}$$

On the right hand side of the Eq. (16), one can recognize the same form of the divergence correction in (14), but now with the factor $\frac{1-\alpha}{2}$ replacing the previous $wgH\left(\frac{\Delta t}{d}\right)^2$. The continuity equation with generalized correction method can be rewritten as:

$$h^{n+1} = h^n - \Delta t H (\nabla_* \cdot \mathbf{v})^n + \frac{d^2(1-\alpha)}{2}\left(\nabla_+^2 - \nabla_\times^2\right) h^n. \tag{17}$$

The value $\alpha = 0.5$ corresponds to the divergence correction factor $w = 0.25$, for the maximum time step allowed by the CFL stability criterion.

Fig. 6 shows experiments performed with the continuity equation correction (17). One can notice a substantial improvement achieved when the gravity wave decoupling is prevented. When compared with the previous experiments (Section 3.2), the height fields become much smoother and the streamline fields get closer to the radial and spiral structures for gravity and gravity-inertia waves, respectively. Still, some shortwave noise can be noticed, especially along x and y axes. For gravity-inertia waves, there is no noise close to the source in the height field, but one can observe an unusual square-like distortion of the streamlines.

4. Mass redistribution technique for preventing grid decoupling

The analysis presented in Section 3 demonstrates that the divergence correction technique reasonably well controls the grid decoupling effect, although it does not completely remove the noise. We therefore propose an alternative method for preventing grid separation on semi-staggered grids attempting to further improve the numerical results.

As stated in [10], a possible way to minimize the effects of grid decoupling under strong forcing is to design parameterization schemes, which would avoid forcing at single grid points. Egger [4] suggested replacing a single point disturbance (by topography) with the influence distributed over four neighboring points. Following similar arguments, we replace fluid height h^n in (7) with the following 5-point average applied not only in the source point but over all h points in the model domain.

$$h^n = (\alpha h + (1-\alpha)\bar{h}^{x'y'})^n. \tag{18}$$

The coefficient α determines an averaging intensity, where $\alpha = 1$ corresponds to no averaging at all, while smaller coefficient provides stronger averaging. It should be noticed that for α less than 0.5 the averaging would change the phase of the shortest waves and will not be considered.

When the proposed technique is applied into the mass continuity equation, the system (7) gets the form:

$$\begin{aligned} u^{n+1} &= u^n - \Delta t g(\overline{\delta_x h}^y)^{n+1}, \\ v^{n+1} &= v^n - \Delta t g(\overline{\delta_y h}^x)^{n+1}, \\ h^{n+1} &= (\alpha h + (1-\alpha)\bar{h}^{x'y'})^n - \Delta t H(\overline{\delta_x u}^y + \overline{\delta_y v}^x)^n + G. \end{aligned} \tag{19}$$

It is useful to perform a stability analysis of the system (19). Assuming the wave-like solution (4), one obtains

$$\begin{aligned} &(\lambda-1)\hat{u} + i2\lambda\mu g \sin\left(\frac{X}{2}\right)\cos\left(\frac{Y}{2}\right)\hat{h} = 0, \\ &(\lambda-1)\hat{v} + i2\lambda\mu g \cos\left(\frac{X}{2}\right)\sin\left(\frac{Y}{2}\right)\hat{h} = 0, \\ &i2\mu H \sin\left(\frac{X}{2}\right)\cos\left(\frac{Y}{2}\right)\hat{u} + i2\mu H \cos\left(\frac{X}{2}\right)\sin\left(\frac{Y}{2}\right)\hat{v} + \left\{\lambda - 1 + (1-\alpha)\left[\sin^2\left(\frac{X}{2}\right) + \sin^2\left(\frac{Y}{2}\right)\right]\right\}\hat{h} = 0. \end{aligned} \tag{20}$$

Satisfying the condition for having non-trivial solutions of the system (20), one gets

$$(\lambda-1)^2(\lambda - 1 + 2B) + (\lambda_1)\lambda 2A = 0, \tag{21}$$

where

$$\begin{aligned} A &= 2gH\mu^2\left[\sin^2\left(\frac{X}{2}\right)\cos^2\left(\frac{Y}{2}\right) + \cos^2\left(\frac{X}{2}\right)\sin^2\left(\frac{Y}{2}\right)\right], \\ B &= \frac{1-\alpha}{2}\left[\sin^2\left(\frac{X}{2}\right) + \sin^2\left(\frac{Y}{2}\right)\right]. \end{aligned} \tag{22}$$

Eq. (21) has three solutions:

$$\begin{aligned} \lambda_1 &= 0, \\ \lambda_{2/3} &= 1 - (A+B) \pm \sqrt{(A+B)^2 - 2A}. \end{aligned} \tag{23}$$

If $(A+B)^2 - 2A \leqslant 0$, the scheme is stable if $B \geqslant 0$, or $\alpha \leqslant 1$. This is satisfied in the entire domain of admissible wave numbers. However, if $(A+B)^2 - 2A > 0$, the stability requires $A + B + \sqrt{(A+B)^2 - 2A} \leqslant 2$, or

$$\sqrt{\frac{A}{2} + B} \leqslant 1. \tag{24}$$

The term on the left hand side of (24) has its maximum in points $(0,\pi)$ and $(\pi,0)$, where $A = 2gH\mu^2$ and $B = \frac{1-\alpha}{2}$. Thus, the criterion (24) gets the form:

$$\sqrt{gH\mu^2 + \frac{1-\alpha}{2}} \leqslant 1 \tag{25}$$

or

$$\sqrt{gH}\mu \leqslant \sqrt{\frac{1+\alpha}{2}}, \tag{26}$$

meaning that this scheme will be numerically stabile for time steps $\sqrt{\frac{1+\alpha}{2}}$ times shorter than the time steps allowed by the CFL criterion for non-modified system (Δt_{nm}), i.e.

$$\Delta t \leqslant \sqrt{\frac{1+\alpha}{2}}\Delta t_{nm}; \quad \Delta t_{nm} = d/\sqrt{gH}. \tag{27}$$

The ratio $\Delta t_{nm}/\Delta t$ depending on coefficient α is presented on Fig. 7, with special emphasis to the area where α is between 0.5 and 1.

Experiments with the new mass redistribution technique are performed using α coefficient values 0.5 and 0.85 (Figs. 8 and 9, respectively). Fig. 8 shows complete absence of a short wave noise, while streamlines have radial and spiral form expected in gravity and gravity-inertia wave experiments, respectively. However, the amplitude of a gravity wave front is damped especially in the experiment with the gravity-inertia waves compared to the same experiment with the divergence correction (note that Figs. 6, 8 and 9 are drawn with the same contour interval). In the case of pure gravity waves experiment, the front is present in the figure but it has smaller gradient if compared to the previous experiment. Also, the introduction of the correction term in the equation requires a reduction of time step interval for about 15% to secure the CFL stability, which makes this approach less computationally efficient. In order to overcome this problem with amplitude attenuation we tested mass redistribution technique with $\alpha = 0.85$. As we can see from Fig. 9, the gravity wave front is present in both cases but with a weak noise in case of pure gravity waves along x and y directions. Compared to the same experiment with the divergence correction, the amount of noise is much smaller while the frontal zone gradients are very similar. In the case of gravity-inertia wave experiment, the noise along x and y directions does not exist, and the gravity wave front is present in both velocity and height field. The contour line of 2.5 is broken only along diagonal directions, which indicate amplitude attenuation again, but to a much smaller extent compared to the experiment with $\alpha = 0.5$. Also, the spiral line in the vicinity of the source does not have the 'perfect' circular form and looks more like the lines in Fig. 6. This could be interpreted

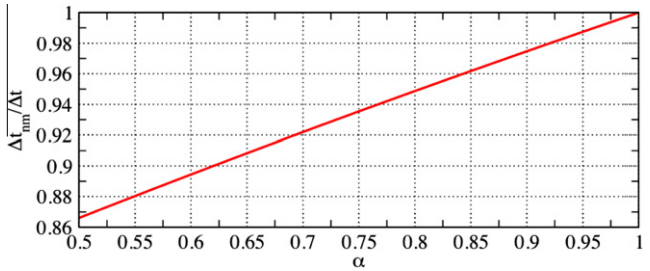

Fig. 7. The ratio between the longest time steps allowed by stability criterion, without any correction and with the mass redistribution applied. Depending on α parameter.

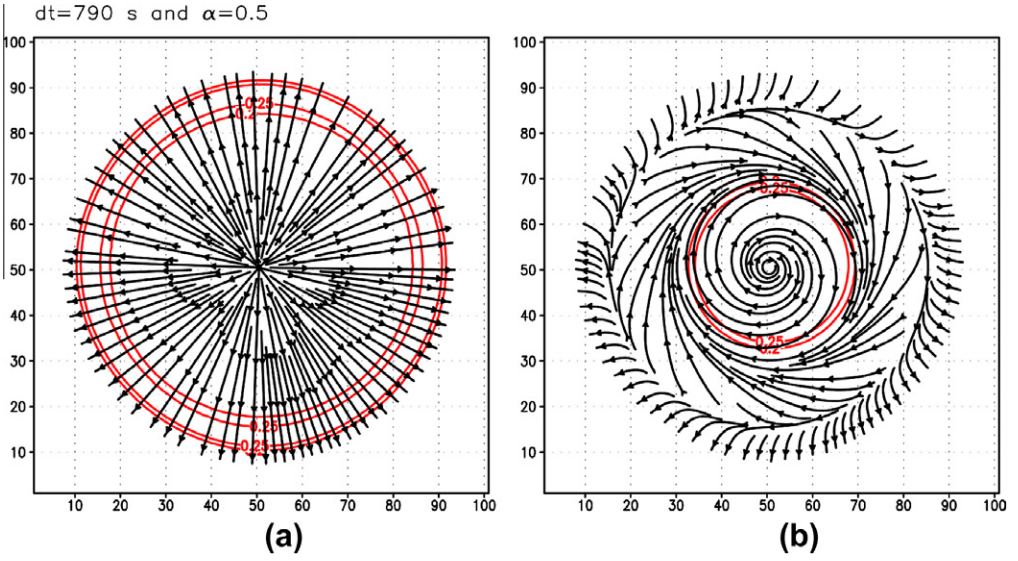

Fig. 8. The same as Fig. 4 but with the mass redistribution applied with a correction factor $\alpha = 0.5$.

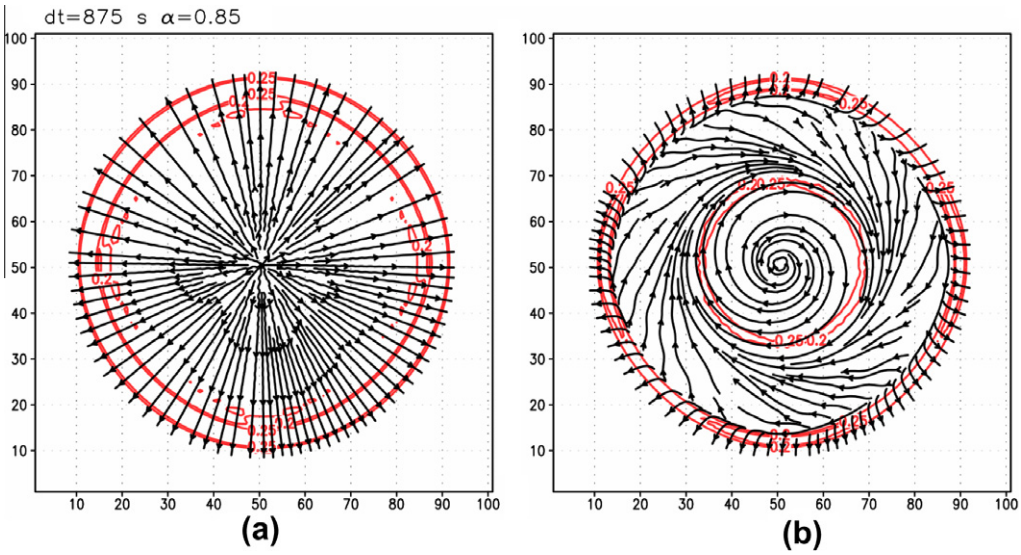

Fig. 9. The same as Fig. 4 but with the mass redistribution applied with a correction factor $\alpha = 0.85$.

as a more realistic feature, because in the case of a constant forcing, the fluid is going through continual geostrophic adjustment and perfect circular form can be associated with geostrophically adjusted flow. The time step in this case is only 5% shorter compared to the experiment with divergence correction, so $\alpha = 0.85$ can be a good compromise concerning the noise removal, correct solution for the wave amplitude and computational efficiency.

6. Conclusions

A numerical scheme has been proposed to prevent the generation of gravity wave decoupling on the two *C* sub-grids of a semi-staggered horizontal grid in hydrodynamic modeling. The scheme establishes efficient connection between gravity wave finite-difference solutions on the sub-grids by a simple averaging of the term in the height tendency in the continuity equation.

To explore capabilities of the new method, tests were performed using a simple shallow water source model developed for the purpose of this study, and results were compared to those made by another method based on correction of the continuity equation. It has been demonstrated that the proposed technique successfully controls the short wave noise originating from wave decoupling that the other numerical schemes do less effectively. The new scheme is time efficient and time explicit, and it can be easily implemented. The proposed method is applicable in hydrodynamic models defined on semi-staggered B or E grids. The method is also successfully applied in hydrology model based on non-linear system of equations [14].

References

[1] W.F. Ames, Numerical Methods for Partial Differential Equations, Nelson, London, 1969.
[2] A. Arakawa, Design of the UCLA General Circulation Model, Numerical Simulation of Weather and Climate, Department of Meteorology, University of California, Los Angeles, Technical Report, No. 7, 1972.
[3] A. Arakawa, V.R. Lamb, Computational design of the basic dynamical processes of the UCLA general circulation model, Methods Comput. Phys. 17 (1977) 173–265.
[4] J. Egger, Mindestgrösse von Gebirgen und Konvektionsgebieten, die in den Modellen der numerischen Vorhersage berücksichtigt werden können, Beitr. Phys. Atmos. 44 (1971) 245–271.
[5] A.J. Gadd, An Economical Explicit Integration Scheme, Meteorological Office Technical Note, 44, 1974.
[6] D. Durran, Numerical Methods for Wave Equations in Geophysical Fluid Dynamics, Springer, New York, 1999.
[7] Z.I. Janjic, A stable centered difference scheme free of the two-grid-interval noise, Mon. Weather Rev. 102 (1974) 319–323.
[8] Z.I. Janjic, Forward-backward scheme modified to prevent two-grid-interval noise and its application in sigma coordinate models, Contrib. Atmos. Phys. 52 (1979) 69–84.
[9] Z.I. Janjic, A nonhydrostatic model based on a new approach, Meteorol. Atmos. Phys. 82 (2003) 271–285.
[10] Z.I. Janjic, F. Mesinger, Response to small-scale forcing on two staggered grids used in finite-difference models of the atmosphere, Q. J. Roy. Meteor. Soc. 115 (1989) 1167–1176.
[11] S.K. Kar, Stable centered-difference schemes based on an unstaggered a grid that eliminate two-grid interval noise, Mon. Weather Rev. 128 (2000) 3643–3653.
[12] F. Mesinger, A method for construction of second-order accuracy difference schemes permitting no false two-grid-interval wave in the height field, Tellus 25 (1973) 444–458.
[13] S. Nickovic, M.B. Gavrilov, I.A. Tosic, Geostrophic adjustment on hexagonal grids, Mon. Weather Rev. 130 (2002) 668–683.

[14] S. Nickovic, G. Pejanovic, V. Djurdjevic, J. Roskar, M. Vujadinovic, HYPROM Hydrology surface-runoff prognostic model, Water Resour. Res. 46 (2010) W11506, doi:10.1029/2010WR009195.
[15] D.A. Randall, Geostrophic adjustment and the finite-difference shallow-water equations, Mon. Weather Rev. 122 (1994) 1371–1377.
[16] T. Torsvik, Ø. Thiem, J. Berntsen, Stability analysis of geostrophic adjustment on hexagonal grids for regions with variable depth, Mon. Weather Rev. 133 (2005) 3335–3344.
[17] F.J.Winninghoff, On the Adjustment Toward a Geostrophic Balance in a Simple Primitive Equation Model with Application to the Problems of Initialization and Objective Analysis, Ph.D. Thesis, Dept. Meteor. Univ. California, Los Angeles, 1968.